Interface Bonds Determined Gas-Sensing of SnO$_2$–SnS$_2$ Hybrids to Ammonia at Room Temperature

Keng Xu,[†,‡] Neng Li,[§] Dawen Zeng,[*,†] Shouqin Tian,[§] Shasha Zhang,[‡] Die Hu,[†] and Changsheng Xie[‡]

[†]State Key Laboratory of Materials Processing and Die & Mold Technology and [‡]Nanomaterials and Smart Sensors Research Lab (NSSRL), Department of Materials Science and Engineering, Huazhong University of Science and Technology (HUST), No. 1037, Luoyu Road, Wuhan 430074, PR China

[§]State Key Laboratory of Silicate Materials for Architectures, Wuhan University of Technology, No. 122, Luo-shi Road, Wuhan 430070, PR China

Ⓢ Supporting Information

ABSTRACT: Unique gas-sensing properties of semiconducting hybrids that are mainly related to the heterogeneous interfaces have been considerably reported. However, the effect of heterogeneous interfaces on the gas-sensing properties is still unclear, which hinders the development of semiconducting hybrids in gas-sensing applications. In this work, SnO$_2$–SnS$_2$ hybrids were synthesized by the oxidation of SnS$_2$ at 300 °C with different times and exhibited high response to NH$_3$ at room temperature. With the increasing oxidation time, the relative concentration of interfacial Sn bonds, O–Sn–S, among the total Sn species of the SnO$_2$–SnS$_2$ hybrids increased first and then decreased. Interestingly, it can be found that the response of SnO$_2$–SnS$_2$ hybrids to NH$_3$ at room temperature exhibited a strong dependence on the interfacial bonds. With more chemical bonds at the interface, the lower interface state density and the higher charge density of SnO$_2$ led to more chemisorbed oxygen, resulting in a high response to NH$_3$. Our results revealed the real roles of the heterogeneous interface in gas-sensing properties of hybrids and the importance of the interfacial bonds, which offers guidance for the material design to develop hybrid-based sensors.

KEYWORDS: hybrid, interfacial bond, room temperature, gas sensor, electron transfer
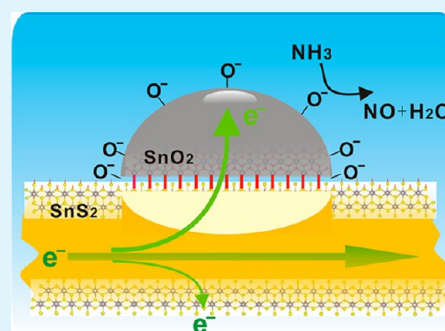
1. INTRODUCTION

Due to the limitation of pristine nanomaterials in gas-sensing performances brought by their own physical and chemical characters,[1] semiconducting hybrids consisting of several different pristine materials have attracted considerable attention for their unique properties which differ substantially from the features of pristine materials.[2,3] Up to now, plenty of hybrids composed of different compositions, morphologies, or dispersion states have been reported with improved gas-sensing behaviors, such as high sensitivity,[4,5] fast response speed,[6] and low working temperature.[7] However, because of the lack of detailed analysis of the mechanism, most of the hybrid studies are strictly empirical, with a trial-and-error type approach in searching suitable hybrids for a given application.[8] When two semiconducting materials with different Fermi energy contact, electrons at the higher energies will flow across the interface to the unoccupied lower-energy states until the Fermi energies across the interface reach a balance. The induced redistributed charge density is the basis of the unique gas-sensing properties.[8] However, a random connection of two different crystals would lead to dangling bonds and voids in the interfacial region,[9] which hinders the charge transfer to a large extent. Since electrons can be trapped in the interfacial dangling bonds, additional energy is needed to cross the electron-depletion layer induced by the interface states,[10] which will reduce the amount of electrons traveling across the interface and further the amount of chemisorbed oxygen.[11] Therefore, a low density of the interface state at the contact interface is much favored to promote the desired electron transfer and further to enhance the gas-sensing performances of hybrids.[12]

Moreover, further studies have indicated that the reconstructed interfacial bonds make the interface itself act as the birthplace of fascinating performances of hybrids.[13−15] For example, owing to the interfacial electronic coupling and charge separations, unique electrical behaviors of SWNT−TiO$_2$ hybrid systems were observed in response to the UV illumination and the subsequent chemical exposure.[16] While a lot of studies have ascribed their superior gas-sensing properties of hybrids to the good interfacial interaction, detailed analysis of the interface is still rare until now. The term of good "interfacial interaction" thus is too vague to indicate the exact interaction mechanism. Therefore, it is important and urgent to clarify the interfacial interaction for designing suitable hybrids with remarkable properties.

On the other hand, among these remarkable gas-sensing properties, low working temperature is much desired, which

can expand the application range of gas sensors and reduce the power consumption. The incorporation of tin oxide with carbon nanostructures, such as graphene or carbon nanotubes, seems to be a promising approach to detect gases at room temperature by an effective electron transfer between metal oxide and carbon nanostructures to enhance the oxygen chemisorption. However, graphene[17] or MWCNTs[18] are mostly metallic and have very high charge carrier concentration, which limits their response to the electron-transfer-induced perturbations. Thus, semiconducting nanomaterials having suitable charge density and intense electron transfer with tin oxide are expected to be used to improve the gas-sensing performances at room temperature.

In the present study, SnS_2, a narrow band gap semiconductor,[19] was chosen to incorporate with SnO_2. Its work function (4.2−4.6 eV)[20] was very close to that of SnO_2 (4.7 eV),[21] making it easy for electrons to travel between SnO_2 and SnS_2, which had been confirmed by Zhang.[22] SnS_2−SnO_2 hybrids were synthesized by oxidizing pristine SnS_2 in air at 300 °C. These hybrids exhibited high response, while neither of its constituent components exhibited response to NH_3 at room temperature. By comparing a series of SnO_2−SnS_2 hybrids oxidized for different times from 0.5 to 4 h, we found that the response of SnO_2−SnS_2 hybrids to NH_3 at room temperature was largely dependent on the chemical bonds at the interface. An new model based on the effects of the interface state on the electron transfer was proposed to understand the gas-response processes of hybrids in detail. Moreover, first-principles calculations revealed that high charge density can result from the reconstructed interfacial bonds due to their narrow band gap, which, also, increased the chemisorbed oxygen dramatically. Our results revealed that it was an effective approach for hybrids to improve gas-sensing properties by increasing the amount of interfacial bonds, which offer guidance for the material design to develop hybrid-based sensors.

2. EXPERIMENTATION

2.1. Preparation of SnS_2 Nanosheets. All the chemical reagents used were of analytical grade and purchased directly from Sinopharm Chemical Reagent Co., Ltd. At first, SnS_2 nanosheets were synthesized through hydrothermal reaction between tin(II) chloride and thiacetamide. In a typical procedure, 4 mmol of $SnCl_2 \cdot 2H_2O$ and 60 mmol of thiacetamide were added into 80 mL of distilled water in order. After vigorous stirring for 30 min, the mixture was transferred into a 100 mL Teflon-lined autoclave, sealed, and heated at 160 °C for 12 h. The system was then allowed to cool to room temperature naturally. The final product was collected by centrifuging the mixture, washing with distilled water and absolute ethanol many times, and then drying in vacuum overnight for further characterization.

2.2. Fabrication of SnO_2−SnS_2-Based Gas Sensors. The SnS_2 sensors fabrication was based on our previous work.[23] First, alumina thin flats (with dimension ca. 6 × 8 mm) were preprinted with the Au interdigital electrodes as the sensor substrate. Second, the as-prepared SnS_2 nanosheets were uniformly dispersed in ethanol by ultrasonication for 15 min to form a suspension. A few drops of the suspension were deposited onto the Au interdigitalted electrodes. After the ethanol evaporated, a SnS_2 film was left on the electrode. Three types of sensors were thus fabricated to explore the gas-sensing mechanism of SnO_2−SnS_2 hybrids: the SnS_2 sensors were directly obtained by drying the SnS_2 films at 100 °C for 12 h to purify the sensors. The other sensors were simply achieved by oxidizing the as-fabricated SnS_2 sensors at 300 °C for different times (i. e., 0.5, 1, 2, 4, and 8 h) in air; the SnO_2 sensors were directly obtained by oxidizing the SnS_2 films at 400 °C for 2 h. For the convenience of description, the SnO_2−SnS_2 hybrids obtained under different oxidation time were

hereinafter named as SnO_2−SnS_2−X, where X denoted the different oxidation time in hours.

2.3. Characterization. The crystal structures of SnS_2, SnO_2−SnS_2, and SnO_2 collected from sensing film were measured on a Philips X'pert X-ray diffractometer with Cu Kα1 radiation in the 2θ range from 10° to 90°. Field-emission scanning electron microscopy (FESEM) was employed to analyze the morphology of the films with an FEI sirion 200 microscope and operated at an acceleration voltage of 20 kV. The transmission electron microscopy (TEM) images of the hybrids were obtained with a Tecnai G2 F30 (FEI, Holland) transmission electron microscope. X-ray photoelectron spectroscopy (XPS) measurements were carried out with a Kratos XSAM800 spectrometer employing Al Kα radiation.

2.4. Gas-Sensing Measurement. In our experiments, the dry air was first introduced into the testing chamber to crowd out the adsorbed water and the residual organic species over a period of time. Then, 10 V bias was applied during the whole testing process. A mixture of dry air and ammonia gas (99.9%, Shanghai Weichuang Standard Gas Analytical Technology Co., Ltd., China) with controlled concentration was introduced for about 200 s, which was controlled by the gas flow rate control module through two parallel mass flow controllers (Beijing Sevenstar Electronics Co. Ltd., China). The device cell was connected with a computer-controlled translation system by the data acquisition device (PCI-6225, National Instrument Co. Ltd.). Most importantly, various parameters were all well controlled by the computer, including the bias voltage, the testing time, and the concentration of the target gas. The gas-sensing sensitivity was assessed through the response value of the photocurrent, which was defined as $S = I_g/I_a$ (where I_g and I_a were the average current amplitude within a cycle in target gas and air, respectively).

3. RESULTS AND DISCUSSION

The crystallographic information has been investigated by XRD, as illustrated in Figure 1. Totally, the increasing oxidation
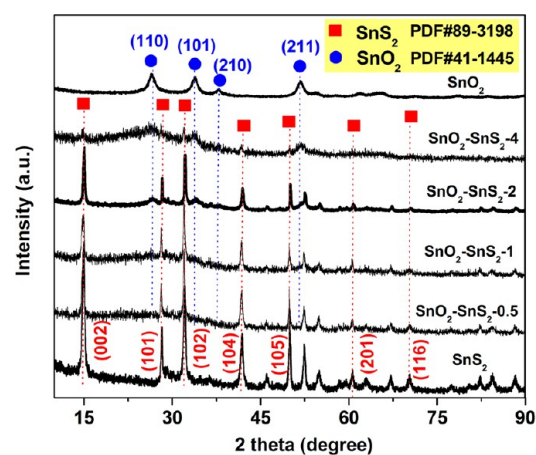

Figure 1. X-ray diffraction patterns of the obtained samples.

time gives rise to an increase in the peak intensity of rutile SnO_2 (JCPDS, No. 41-1445) at the price of decreasing the peak intensity of SnS_2 (JCPDS, No. 89-3198), indicating that the SnS_2 gradually transforms to rutile SnO_2 with the prolonged oxidation time. According to the relative ratio of diffraction intensity $(I_{SnO2(110)})/(I_{SnS2(101)})$, the relative content of SnO_2 to SnS_2 is 0%, 6.2%, 9.3%, and about 100% corresponding to SnO_2−SnS_2-0.5, SnO_2−SnS_2-1, SnO_2−SnS_2-2, and SnO_2−SnS_2-4, respectively. This indicates that the percent composition of SnS_2 in the SnO_2−SnS_2 hybrid systems keeps increasing from SnO_2−SnS_2-0.5 to SnO_2−SnS_2-4. Moreover, no other impurity diffraction peaks are discovered in all of these samples, which confirms the high purity of the products.
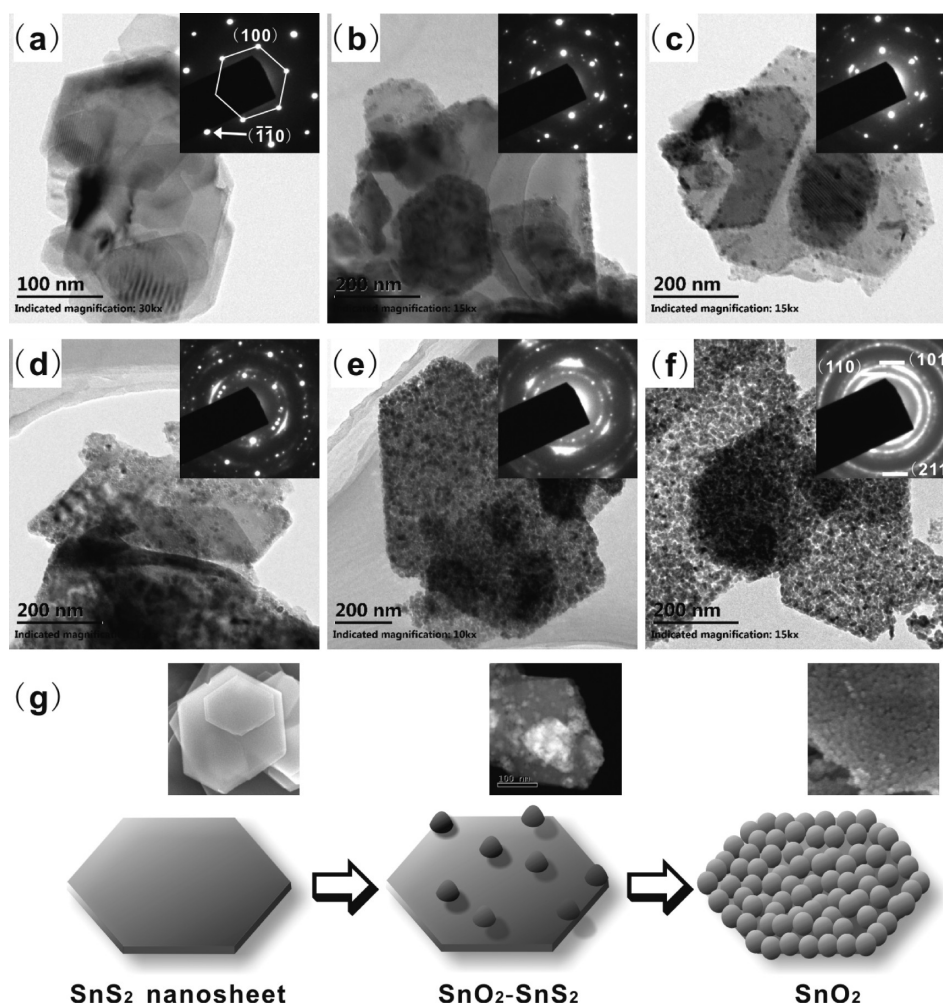
Figure 2. SEM images of (a) SnS_2, (b) SnO_2-SnS_2-0.5, (c) SnO_2-SnS_2-1, (d) SnO_2-SnS_2-2, (e) SnO_2-SnS_2-4, and (f) SnO_2. The insets are the corresponding SAED patterns. (g) Schematic diagram illustrating the morphology evolution processes.

Low-magnification SEM images of pristine SnS_2, SnO_2-SnS_2-1, and SnO_2 are presented in Figure S1 (Supporting Information) to investigate the morphological evolution with the oxidation process. Both SnS_2 (Figure S1a, Supporting Information) and SnO_2-SnS_2 (Figure S1b, Supporting Information) show a typical sheet-like morphology with lateral size ranging from 20 nm to 1 μm and a thickness of dozens of nanometers. Figure S1c (Supporting Information) reveals that the SnO_2 nanosheets are composed of fine nanoparticles. A more detailed morphological evolution process of SnO_2-SnS_2 hybrids as a function of oxidation time is shown in Figure 2. As can be seen, pristine SnS_2 (Figure 2a) consists of hexagonal nanosheets with smooth surfaces, while SnS_2-SnO_2 hybrids (from Figure 2b to Figure 2e) consist of both hexagonal nanosheets and fine nanoparticles. The structure of nanoparticles is rutile SnO_2 as confirmed by the ring electron diffraction patterns (inset) which can be found even in the sample of SnO_2-SnS_2-0.5. When the oxidation time increases from 0.5 to 4 h, the amount of SnO_2 nanoparticles gradually increases, which is in accord with the XRD results. However, the SnO_2 nanoparticles are dispersed on the surface of SnS_2 nanosheets without any pores at the beginning of the oxidizing process. When the oxidation time is higher than 2 h, SnO_2 nanoparticles tend to grow in colonies. And pores between SnO_2 nanoparticles, and SnS_2 nanosheets are observed from

Figure 2d and Figure 2e, which can be explained by the minimization of surface energy.

Two main processes are concluded in the morphological evolution as shown in Figure 2g. At first, SnO_2 nanoparticles nucleate on the surface of SnS_2 nanosheets directly. To minimize the surface energy associated with the unsatisfied bonds, the chemical bonds between SnO_2 and SnS_2 are formed. Therefore, the interfacial bonds increase with the increasing amount of SnO_2 nanoparticles. However, with the increased oxidation time, the growth process of SnO_2 nanoparticles dominates the nucleation process, in which surface energy is mainly minimized by forming chemical bonds between SnO_2 and SnO_2. Namely, the SnO_2 nanoparticles tend to grow in colonies and "weld" together.[24] The formation of chemical bonds between SnO_2 and SnS_2, as is not a main mode to minimize the surface energy, gives way to the growth process of SnO_2 nanoparticles. Moreover, with the growth of SnO_2 nanoparticles, the SnS_2 nanosheets can fully transform to SnO_2 in some parts of the nanosheets. In this case, the amount of chemical bonds between SnO_2 and SnS_2 decreases, and the pores between them start to appear with the increased oxidation time.

To further verify the speculation, a detailed analysis of interfacial evolution is performed by means of atomic resolution high-angle annular dark field (HAADF) STEM in
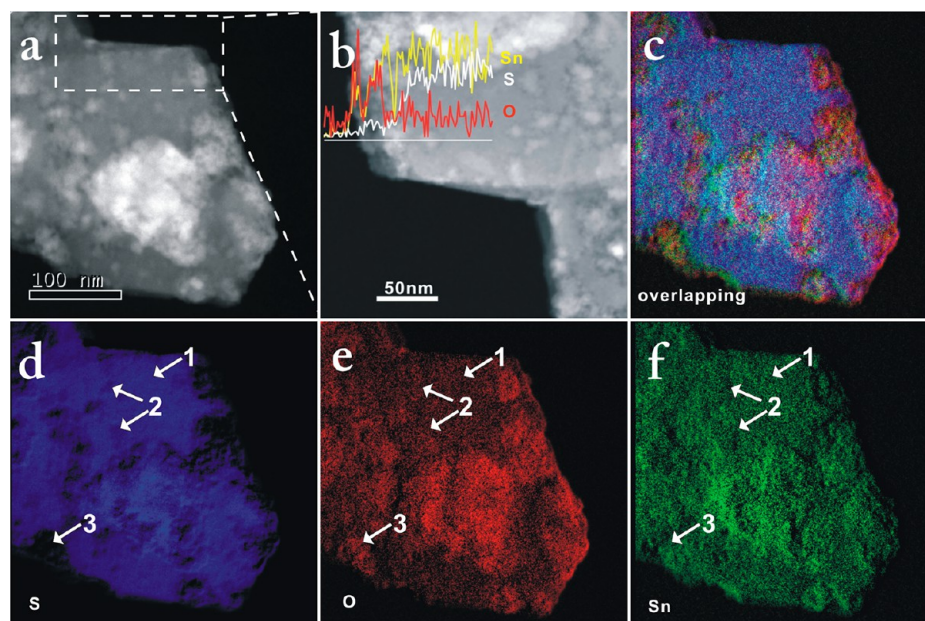
Figure 3. (a) HAADF STEM image of SnO_2−SnS_2-1, (b) STEM-EDX concentration line profiles of Sn, S, and O measured along the white straight line, (c) EELS overlaid image of Sn, S, and O, (d−f) EELS images of each element corresponding to S, O, and Sn, respectively.

combination with EDS and electron energy loss spectroscopy (EELS) as shown in Figure 3. Consistent with the TEM results, SnS_2−SnO_2-1 contains nanosheets which are decorated with some nanoparticles (Figure 3a). EDS elemental mapping profiles (Figure 3b) of Sn, S, and O also reveal that the composition of the nanosheets and nanoparticles are Sn/S and Sn/O, respectively. The EELS mappings (Figure 3c) show that the distribution of Sn elements (green) is homogeneous and continuous, whereas O elements (red) and S elements (blue) are isolated and discontinuous. There are three kinds of regions (bright blue as region 1, deep blue as region 2, and black as region 3) in the S elements mapping of Figure 3d (arrow), corresponding to three regions (black-red as region 1, deep-red as region 2, and bright-red as region 3) in the O elements mapping of Figure 3e. These three regions represent different contact statuses between SnO_2 and SnS_2, which also reveals the interfacial evolution between SnS_2 and SnO_2. Region 1 consists of a lot of S element (bright-blue) and little O element (black-red), indicating the purity of the SnS_2 surface without SnO_2 nanoparticles and chemical bonds between SnO_2 and SnS_2. And a moderated amount of the S element (deep-blue) and O element (deep-red) coexist in region 2 where a large amount of interfacial bonds can be induced to minimize the surface energy. Region 3 only consists of the O element (bright-red) without the S element (black) due to the complete transformation of SnS_2 to SnO_2 in this region during the growth process. The amount of chemical bonds between SnS_2 and SnO_2 thus also decreases. As discussed above, with the increased oxidation time, region 1, region 2, and region 3 may dominate in the SnO_2−SnS_2 hybrid systems, respectively. The amount of chemical bonds at the interface, therefore, may increase first and then decrease.

To further explore the evolution of interfacial bonds with the oxidation time, XPS measurement is performed.[25] Detailed information on the chemical state of these elements is shown in the high-resolution XPS spectra of the O 1s, Sn $3d_{5/2}$, and S 2p. The O 1s spectra in Figure 4a can be deconvoluted into four contributions using the Gaussian−Lorentzian profile. The

peaks at 531.1 eV are ascribed to Sn−O−Sn lattice species without oxygen defects, and the features at 530.1 eV are assigned to the oxygen vacancies (V_o) in the oxide lattices.[26] The peak at 532.3 eV could be associated with the oxide in hydroxide, and the peak with binding energy of 534.1 eV is ascribed to H_2O. On the basis of the area ratio of O species from the fitted peaks, the fraction of the 531.1 eV peak increases at first and then decreases with the increased oxidation time.[27,28] The SnO_2−SnS_2-1 exhibits the highest intensity of this peak which may be due to its largest electronic interface region between SnS_2 and SnO_2 where lattice defects will form to compensate the lattice mismatch-induced strain.[29] This assumption can also be confirmed from the analysis of Sn $3d_{5/2}$ spectra as shown in Figure 4b. The Sn $3d_{5/2}$ spectra exhibit three peaks at 487.4, 486.9, and 486.0 eV. The former two peaks are assigned to Sn^{4+} and Sn^{2+}, respectively.[30] The latter peak whose binding energy is larger than that of Sn^0 (484.8 eV)[31] can be assigned to S−Sn−O, which results from the chemical bonds between SnS_2 and SnO_2 (Figure 4c). On the basis of the area ratio of Sn species from the fitted peaks, the intensities of both the Sn^{2+} and S−Sn−O peaks increase at first and then decrease with the increased oxidation time as shown in Figure 4c, which is the same as the change trend of O 1s spectra at 531.1 eV. In addition, this trend is also confirmed by S 2p spectra as shown in Figure S2 (Supporting Information). The S 2p spectrum of pristine SnS_2 has a S $2p_{3/2}$ peak at 162.2 eV and a S $2p_{1/2}$ peak at 163.4 eV.[32] However, compared with the pristine SnS_2, the S 2p peaks in SnO_2−SnS_2-0.5, SnO_2−SnS_2-1, SnO_2−SnS_2-2, and SnO_2−SnS_2-4 are shifted to the low binding energy. Zhang[33] has ascribed this binding energy shift to the changed electron concentration of SnS_2 due to electron transfer between two semiconductors with different Fermi energy levels. In our case, this binding energy shift of SnS_2 may also result from the changed electron concentration of SnS_2, which needs further research. Most important, there is another weak peak at 161.1 eV in SnO_2−SnS_2-0.5 and SnO_2−SnS_2-1, which may be ascribed to the bonds with interfacial Sn ions. As the interfacial
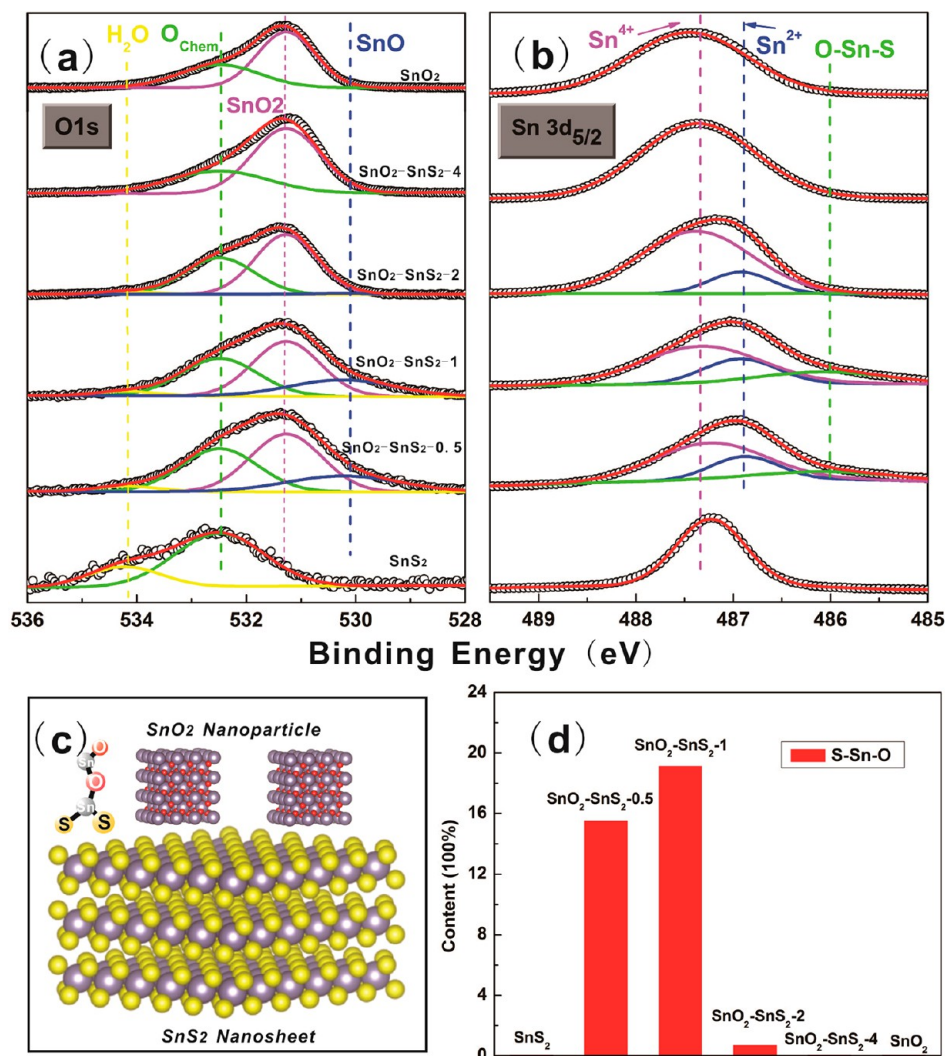
Figure 4. High-resolution spectra of (a) O 1s and (b) Sn $3d_{5/2}$ of SnS_2, SnO_2−SnS_2-0.5, SnO_2−SnS_2-1, SnO_2−SnS_2-2, SnO_2−SnS_2-4, and SnO_2 from the bottom. (c) Schematic illustration of SnO_2−SnS_2 contacts. (d) Semiquantitative analysis of the fraction of O−Sn−S among the total of O−Sn−O, O−Sn−S, and O−Sn.
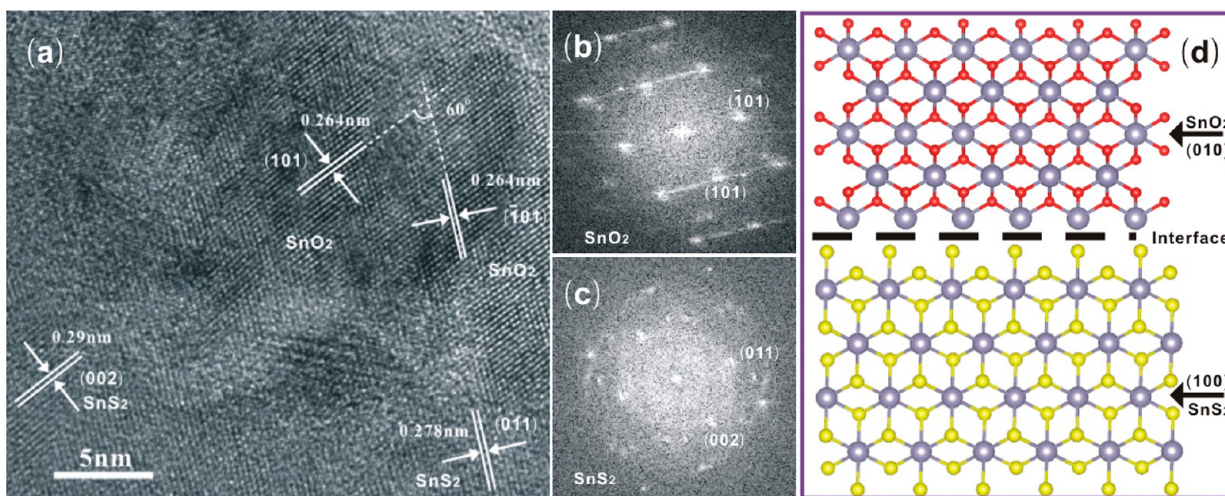
Figure 5. (a) HRTEM image of SnO_2 on the surface of SnS_2 (left), (b) FFT image of SnO_2, (c) FFT image of SnS_2, and (d) the side view of the structure model of the interface between SnO_2 and SnS_2.

bonds appear, the binding energy of Sn ions in S−Sn−O bonds is different from that of S−Sn−S. Therefore, the binding energy

of S ions is changed at the same time. In addition, with the increased oxidation time, the peak intensity of interfacial bonds
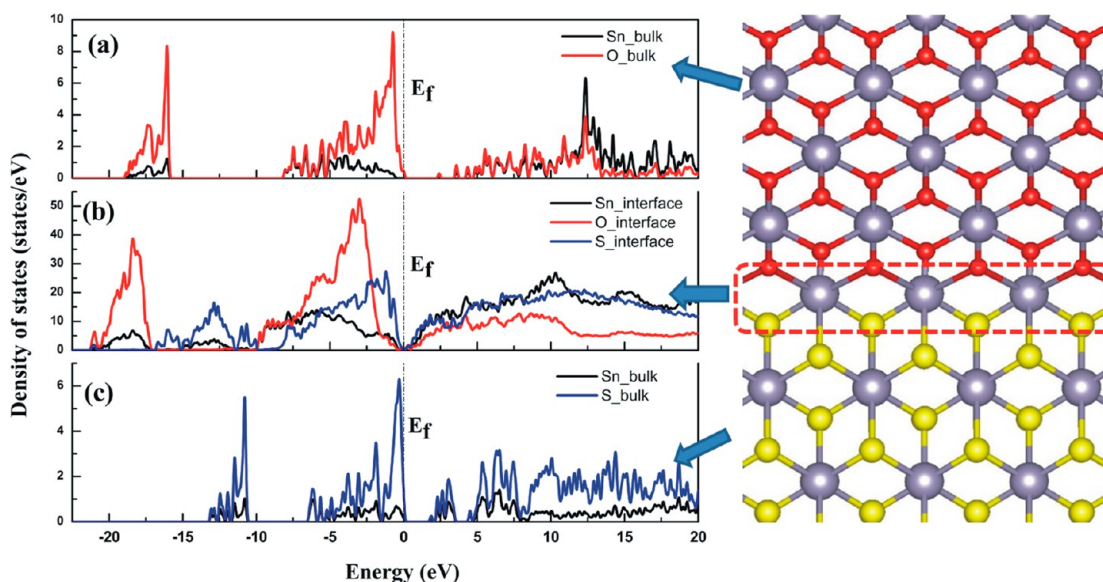
Figure 6. (a–c) DFT-calculated total and local density of states of the SnO$_2$–SnS$_2$ interface.

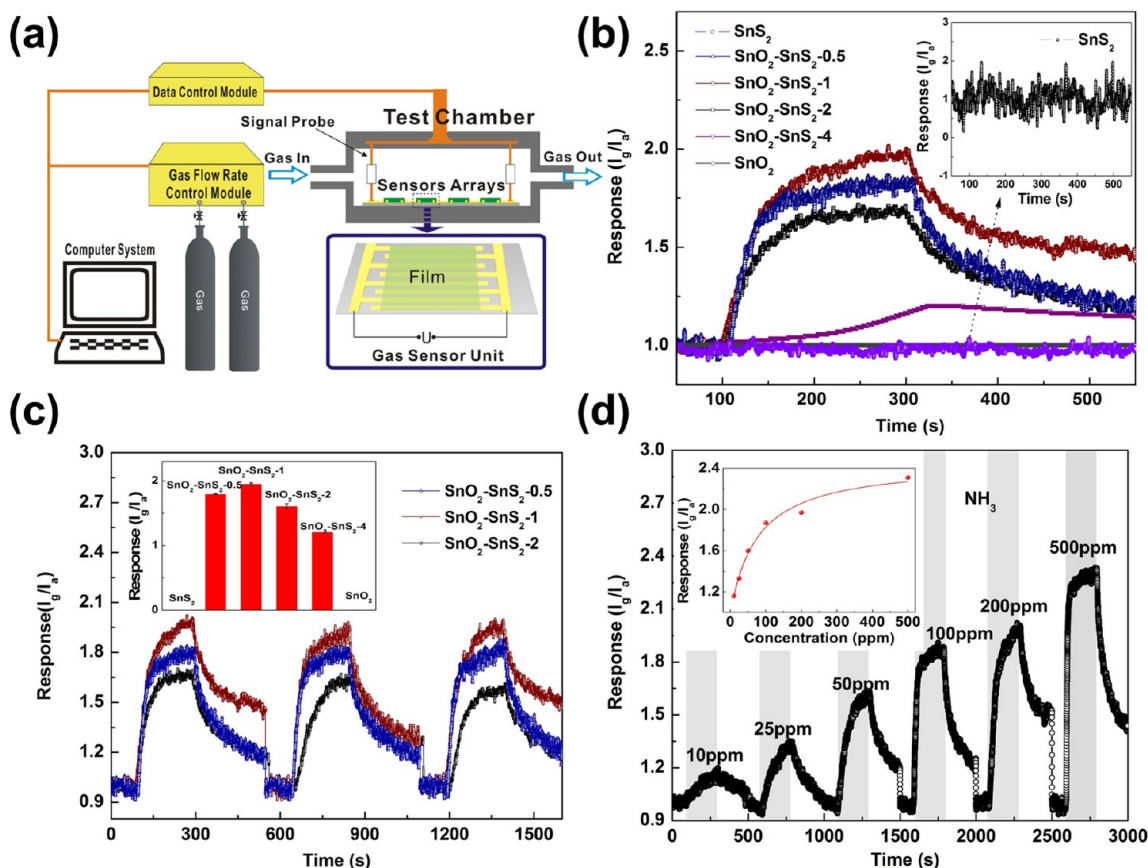**Figure 7.** (a) Schematic diagram illustrating the gas-sensing test platform. (b) Dynamic response-recovery curves of the obtained samples to NH$_3$ with 100 ppm at room temperature. The inset shows a larger version of SnS$_2$. (c) The inset shows the response of the obtained samples to a NH$_3$ with 100 ppm. Repetitive dynamic response–recover curves of SnO$_2$–SnS$_2$-0.5, SnO$_2$–SnS$_2$-1, and SnO$_2$–SnS$_2$-2. (d) The response-recovery curves of SnO$_2$–SnS$_2$-1 to NH$_3$ in the concentration range from 10 to 500 ppm. The inset shows the response as a function of NH$_3$ concentration.

also increases first and then decreases. These results demonstrate that the amount of chemical bonds at the interface increases at first and exhibits the highest in SnO$_2$–SnS$_2$-1. After that, the amount of interfacial bonds decreases with the increased oxidation time.

To further explore the interfacial electronic properties, the crystal structure of the interface is characterized by the lattice-resolved TEM in Figure 5. It reveals that the SnO$_2$ nanoparticles grow on the SnS$_2$ nanosheets along a particular direction as shown in Figure 5a where the plane (101) SnO$_2$ is parallel to the plane (002) SnS$_2$ and the plane (−101) SnO$_2$ is

parallel to the plane (011) SnS_2. This result is also confirmed by the fast Fourier transform (FFT) as shown in Figure 5b and Figure 5c. Thus, the crystallographic orientation relationship can be expressed as (010) SnO_2/(100) SnS_2. Figure 5d depicts the side view of the interface between the SnO_2 and SnS_2 models along this direction. The best matching of a crystal with an adjacent crystal is achieved when the interface between the two crystals has minimal interfacial energy, resulting in interfacial bonds. The DFT-calculated total density of states (TDOS) and local density of states (LDOS) projected onto the different layers of the interface model are applied as shown in Figure 6. The labels marked "bulk SnO_2" and "bulk SnS_2" mean the projections on the layers far from the interface, so the bonding environment is almost identical to that in the bulk. As Figure 6 shows, there is a significant decrease of band gap in the heterojunction compared to those of bulk SnO_2 and SnS_2, which can be attributed to lattice stress and defect states in the SnO_2/SnS_2 interface. This result suggested that the SnO_2/SnS_2 heterojunction can act as an antenna to improve gas-sensing properties, which is consistent with our experimental measurement of gas-sensing performances in the following section. Moreover, the bond distance and bond order values are further calculated as shown in Figure S3 (Supporting Information), and the results are presented in Table S1 (Supporting Information). Obviously, the bond length close to the interface is longer, while the bond order is smaller than that in the bulk. These results indicate that the binding energy of O−Sn−S is different from that of other Sn ions, which is well matching the XPS results.

Gas-sensing properties were tested in a steel-made dark chamber as illustrated in Figure 7a. Since the interface state between SnS_2 and SnO_2 has a great influence on the charge density, the as-synthesized SnO_2−SnS_2 hybrids with good electronic contact are expected to show good gas-sensing performance. The gas responses to NH_3 (100 ppm) are measured at room temperature (298 k) in dark conditions. From these dynamic response−recovery curves shown in Figure 7b, it can be clearly observed that the output signal currents of SnO_2−SnS_2-0.5, SnO_2−SnS_2-1, SnO_2−SnS_2-2, and SnO_2−SnS_2-4 increase upon the injection of NH_3 and decrease after NH_3 is released, indicating the n-type response of the SnO_2−SnS_2 hybrids. The responses of these samples to NH_3 are significantly different. Pristine SnS_2 and SnO_2 are not sensitive to NH_3 here in our case, while SnO_2−SnS_2 hybrids show identical behavior of high response due to the interfacial bonds. The I_g/I_a (represent the current in NH_3 and dry air, respectively) values are used to measure the responses of the sensors as shown in the inset of Figure 7c. Obviously, the response increases at first and then decreases from SnO_2−SnS_2-0.5 to SnO_2−SnS_2-4, reaching a maximum for SnO_2−SnS_2-1. The same change trend with the evolution of chemical bonds at the interface indicates that the gas-sensing activity is mostly dependent on the amount of chemical bonds at the interface.

Owing to its intimate electronic contact, SnO_2−SnS_2-0.5, SnO_2−SnS_2-1, and SnO_2−SnS_2-2 also show other excellent gas-sensing behaviors, such as good reproducibility and quick response. Figure 7c shows the typical response recovery characteristics of SnO_2−SnS_2-0.5, SnO_2−SnS_2-1, and SnO_2−SnS_2-2 to 100 ppm of NH_3 which appear fairly reproducible. Figure 7d illustrates the response-recovery characteristics of SnO_2−SnS_2-1 to NH_3 with concentrations of 10, 25, 50, 100, 200, and 500 ppm at room temperature. The sensor exhibits both excellent sensitivity and good reproducibility when

exposed to various NH_3 concentrations. When exposed to 10 ppm of NH_3, the response is about 1.16, indicating that gas response can be achieved in detecting low concentration NH_3 using SnO_2−SnS_2 hybrids as gas-sensing material. Furthermore, the sensor shows a quick response at room temperature. When exposed to 500 ppm of NH_3, the response time (defined as the time required to reach 90% of the final equilibrium value) is only 11 s, which is much shorter than other NH_3 gas sensors reported.[34] In order to demonstrate the potential use of hybrids in high response and selective gas sensing, we also measure the gas responses to HCHO, CO, C_6H_6, and H_2S which exhibit no response to these gases, indicating the high selectivity to NH_3 of SnO_2−SnS_2-1.

In addition, to eliminate the effect of composition on the gas-sensing performance, physical mixed SnO_2−SnS_2 hybrids were prepared. The relative content of SnO_2 and SnS_2 was obtained by the element ratio of oxygen and sulfur by XPS. Three physical mixed samples with relative content corresponding to the SnO_2−SnS_2-0.5, SnO_2−SnS_2-1, and SnO_2−SnS_2-2 were conducted. These newly as-prepared samples were named as PM-SnO_2−SnS_2-0.5, PM-SnO_2−SnS_2-1, and PM-SnO_2−SnS_2-2, respectively. The morphology of PM-SnO_2−SnS_2-1 is shown in Figure S4 (Supporting Information). Both SnO_2 and SnS_2 can be observed with the same size as that of SnO_2−SnS_2-1. However, all of them exhibited no response to NH_3. The typical response−recovery curves are shown in Figure S5 (Supporting Information). These results further confirm the important role of interfacial bonds between SnO_2 and SnS_2 in the gas sensing performance for NH_3.

The commonly accepted gas-sensing mechanism for n-type semiconducting metal oxides such as SnO_2 at high work temperature involves an adsorption−oxidation−desorption process in which chemisorbed oxygen plays a crucial role.[35] When SnO_2 is exposed to air, oxygen could trap electrons from the conduction band of SnO_2 to form adsorbed oxygen species (O_2^-, O^-, O^{2-}), which results in a decrease in the conductivity of SnO_2. When the sensor is exposed to reductive NH_3, it would react with the adsorbed oxygen species and release electrons into SnO_2, thereby increasing the conductivity of SnO_2. As a result, the resistance change can be found.[36] Obviously, the amount of chemisorbed oxygen on the surface is critical for the variation in resistance and the performance of the sensor. In our case, both pristine SnS_2 and SnO_2 exhibit no response to NH_3 at room temperature. This is due to the small coverage of chemisorbed oxygen and a small change in sensor conductivity which is below the detection limit. However, at room temperature, it is feasible for SnO_2 to have a high response to NH_3 or NO_2 once high charge density is generated by UV illumination[37] or by functionalization with CNTs or graphene. Therefore, the phenomenon that the response of the SnO_2−SnS_2 hybrids to NH_3 not only is detectable but also increases with the amount of chemical bonds at the interface can be ascribed to the increased charge density by the interfacial bondings.[1]

In the SnO_2−SnS_2 hybrid system, the work function of SnO_2 is lower than that of SnS_2, leading to the electron transfer from SnS_2 to SnO_2 upon their contact. Electrons of SnS_2 can travel to the surface of SnO_2 and be trapped by oxygen molecules. For simplicity we assume that the electrons of the chemisorbed oxygen on the surface of SnO_2 mainly come from SnS_2, which refers to the electron transfer from SnS_2 to SnO_2. The electrons of SnO_2 are neglected since pristine SnO_2 exhibits no response to NH_3. Now the amount of chemisorbed oxygen on the
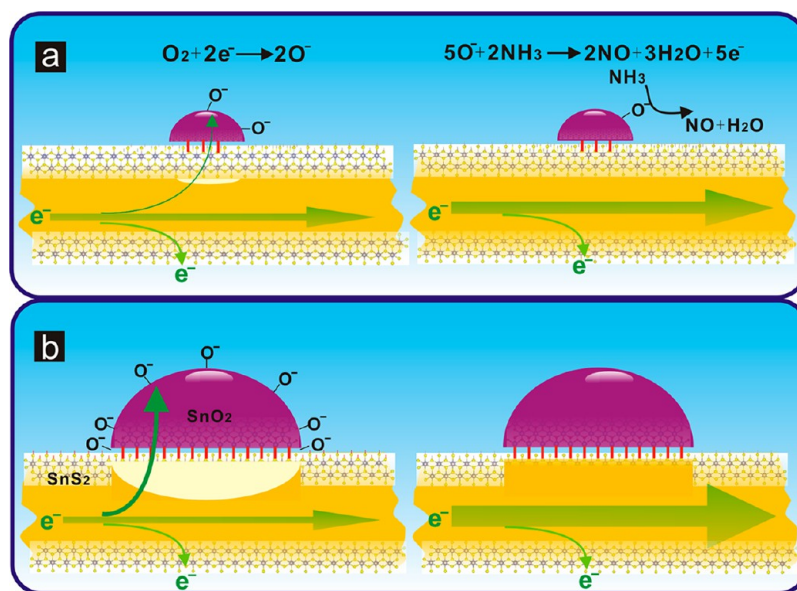
Figure 8. Schematic of the SnO₂–SnS₂ hybrid with a (a) small amount and (b) large amount of chemical bonds at the interface and their corresponding gas-sensing process.

surface of SnO_2 is thus determined by the density of foreign electrons from SnS_2. On the other hand, due to the dangling bonds at the interface, the electric charge can also be trapped at the interface region. In this case, besides a electron-depletion layer formed by a potential difference between SnO_2 and SnS_2, an additional electron-depletion layer also exists in the interface region due to the trapped electrons at the interfacial dangling bonds.[38] This potential barrier height of the electron-depletion layer can be formulated[39]

$$\psi = \frac{eN_{d1}\omega^2}{2\varepsilon} \tag{1}$$

Here N_{d1} is the donor density, and ε is the dielectric constant of SnS_2. ω is the thickness of the electron-depletion layer of SnS_2, which is given by

$$\omega = \frac{(Q_2 + Q_i)}{N_{d1}} \tag{2}$$

where Q_2 and Q_i are the density of chemisorbed oxygen on the surface of SnO_2 and the interface state density, respectively. From these equations, the ψ is presented by

$$\psi = \frac{e(Q_2 + Q_i)^2}{2\varepsilon N_{d1}} \tag{3}$$

Now the amount of foreign electrons can be calculated by

$$C = V_2 N_{d1} \exp\left(-\frac{\psi}{kT}\right) = V_2 N_{d1} \exp\left[-\frac{e(Q_2 + Q_i)^2}{2\varepsilon kT N_{d1}}\right] \tag{4}$$

Here k and T are Boltzmann constant and temperature, respectively. The V_2 is the volume of SnO_2 grains. In order to obtain the relationship between Q_2 and Q_i, another equations is needed

$$C = Q_2 S_2 \tag{5}$$

where S_2 is the surface area of SnO_2 grains. From eqs 4 and 5, we obtain

$$V_2 N_{d1} \exp\left[-\frac{e(Q_2 + Q_i)^2}{2\varepsilon kT N_{d1}}\right] = Q_2 S_2 \tag{6}$$

Thus, a relationship between the density of chemisorbed oxygen and the interface state is established. For simplicity we assume the SnO_2 grains are all hemispheres. One obtains

$$r_2 N_{d1} \exp\left[-\frac{e(Q_2 + Q_i)^2}{2\varepsilon kT N_{d1}}\right] = 3Q_2 \tag{7}$$

Here r_2 is the radius of SnO_2 hemispheres. From this formula, we can see that the density of chemisorbed oxygen would increase if the density of the interface state decreases and vice versa. Since the explicit function of Q_2 is hard to express, two extreme cases are discussed here to illustrate the change trend semiquantitatively. The first is neglecting the interface state with the assumption of the perfect contact between SnO_2 and SnS_2 where $Q_i = 0$ is obtained. Now this formula can be simplified as

$$\exp(-eQ_2^2 - \ln Q_2) = 3\frac{e^{-2kT\varepsilon r_2 N_{d1}}}{r_2 N_{d1}} \tag{8}$$

N_{d1} is the donor density of SnS_2, and r_2 is the radius of SnO_2 hemispheres. Apparently, Q_2 depends on the donor density of SnS_2 and interfacial contact area. Thus, the density of chemisorbed oxygen increases with the increased donor density of SnS_2 or interfacial contact area, which is consistent with the usually observed sintering-neck model.[40]

The second extreme case is that the Q_i is much higher than Q_2. Then another equation thus can be obtained

$$3Q_2 = r_2 N_{d1} \exp\left(-\frac{eQ_i^2}{2\varepsilon kT N_{d1}}\right) \tag{9}$$

Note that Q_2 is proportional to the exponential $-Q_i^2$. The Q_2 thus is promoted drastically with the decreased Q_i but is only slightly dependent on N_{d1}. This indicates that the density of chemisorbed oxygen is very dependent on the chemical bonds

at the interface which can reduce the density of the interface state. These conclusions are well consistent with our experimental results.

Thus, from the analysis of these two cases, we can obtain that the role of the interface in the gas-sensing properties is largely dependent on the amount of chemical bonds at the interface as illustrated in Figure 8. When the amount of chemical bonds at the interface is very little (Figure 8a), electrons should travel across the electron-depletion layer induced by the interface state. Owing to the high potential barrier, the amount of electrons that can travel across the electron-depletion layer is very small, which leads to small amount of chemisorbed oxygen on the surface of SnO_2. With the decreasing amount of chemical bonds at the interface, the effect of the interface becomes distinct. From eq 9, the density of chemisorbed oxygen can increase dramatically by adding a small amount of interfacial bonds. Thus, the gas-sensing properties of hybrids are largely dependent on the amount of interfacial bonds in this case. Moreover, the reconstructed interfacial bonds can also make the interface show excellent gas-sensing performances. High density of charge and chemisorbed oxygen can be induced due to its narrow band gap from the result of first-principles calculations, which also plays a key role in increasing the response of SnO_2-SnS_2 hybrids dramatically.

When the electrical contact between SnO_2 and SnS_2 is perfect (Figure 8b), the potential barrier induced by the interface state is low, making the amount of electrons that can travel across the interface become very large. The density of chemisorbed oxygen is thus mainly dependent on the donor density of SnS_2 or interfacial contact area from eq 8, which is consistent with the usually observed sintering-neck model of the homojunction.

4. CONCLUSIONS

SnO_2-SnS_2 hybrids were synthesized by the oxidation of SnS_2 which exhibited high response to NH_3 at room temperature. We found that the response of SnO_2-SnS_2 hybrids to NH_3 exhibited a strong dependence on the amount of interfacial bonds. A new model based on the effects of the interface state on the electron transfer was proposed, which revealed that the response of hybrids increased with the amount of chemical bonds at the interface. Moreover, first-principles calculations reveal that high response can result from the reconstructed interfacial bonds due to their narrow band gap. Our results revealed that it was an effective approach for hybrids to improve gas-sensing properties by increasing the interfacial bonds, which can offer guidance for the material design to develop hybrid-based sensors.

ASSOCIATED CONTENT

Ⓢ Supporting Information

The low-magnification SEM images, high-resolution spectra of S 2p, calculated bond properties, TEM image of PM-SnO_2–SnS_2-1, and the response–recovery curve of PM-SnO_2–SnS_2-1 to 100 ppm of NH_3. The Supporting Information is available free of charge on the ACS Publications website at DOI: 10.1021/acsami.5b01856.

AUTHOR INFORMATION

Corresponding Author
*Tel.: +86-027-87559835. Fax: +86-027-87543778. E-mail: dwzeng@mail.hust.edu.cn (D. Zeng).

Notes

ACKNOWLEDGMENTS

REFERENCES

(1) Yamazoe, N.; Tamaki, J.; Miura, N. Role of Hetero-junctions in Oxide Semiconductor Gas Sensors. *Mater. Sci. Eng. B* **1996**, *41*, 178–181.

(2) Lyson-Sypien, B.; Czapla, A.; Lubecka, M.; Kusior, E.; Zakrzewska, K.; Radecka, M.; Kusior, A.; Balogh, A. G.; Lauterbach, S.; Kleebe, H.-J. Gas Sensing Properties of TiO_2-SnO_2 Nanomaterials. *Sens. Actuators, B* **2013**, *187*, 445–454.

(3) Wang, Z. Q.; Wang, J.; Sham, T. K.; Yang, S. G. Tracking The Interface of An Individual ZnS/ZnO Nano-Heterostructure. *J. Phys. Chem. C* **2012**, *116*, 10375–10381.

(4) Chen, X.; Guo, Z.; Xu, W. H.; Yao, H. B.; Li, M. Q.; Liu, J. H.; Huang, X. J.; Yu, S. H. Templating Synthesis of SnO_2 Nanotubes Loaded With Ag_2O Nanoparticles and Their Enhanced Gas Sensing Properties. *Adv. Funct. Mater.* **2011**, *21*, 2049–2056.

(5) Yu, J. H.; Choi, G. M. Electrical and CO Gas Sensing Properties of ZnO–SnO_2 Composites. *Sens. Actuators, B* **1998**, *52*, 251–256.

(6) Huang, Q. W.; Zeng, D. W.; Li, H. Y.; Xie, C. S. Room Temperature Formaldehyde Sensors With Enhanced Performance, Fast Response and Recovery Based on Zinc Oxide Quantum Dots/Graphene Nanocomposites. *Nanoscale* **2012**, *4*, 5651–5658.

(7) Russo, P. A.; Donato, N.; Leonardi, S. G.; baek, S.; Conte, D. E.; Neri, G.; Pinna, N. Room-Temperature Hydrogen Sensing with Heteronanostructures Based on Reduced Graphene Oxide and Tin Oxide. *Angew. Chem.* **2012**, *124*, 11215–11219.

(8) Miller, D. R.; Akbar, S. A.; Morris, P. A. Nanoscale Metal Oxide-Based Heterojunctions for Gas Sensing: A Review. *Sens. Actuators, B* **2014**, *204*, 250–272.

(9) Liu, H. W.; Zheng, Z. F.; Yang, D. J.; Ke, X. B.; Jaatinen, E.; Zhao, J. C.; Zhu, H. Y. Coherent Interfaces Between Crystals in Nanocrystal Composites. *ACS Nano* **2010**, *4*, 6219–6227.

(10) Park, S.; Ko, H.; Kim, S.; Lee, C. Role of the Interfaces in Multiple Networked One-Dimensional Core–Shell Nanostructured Gas Sensors. *ACS Appl. Mater. Interfaces.* **2014**, *6*, 9595–9600.

(11) Yamazoe, N.; Shimanoe, K.; Sawada, C. Contribution of Electron Tunneling Transport in Semiconductor Gas Sensor. *Thin Solid Films* **2007**, *515*, 8302–8309.

(12) Jeong, S.; Choe, M.; Kang, J. W.; Kim, M. W.; Jung, W. G.; Leem, Y. C.; Chun, J.; Kim, B. J.; Park, S. J. High-Performance Photoconductivity and Electrical Transport of ZnO/ZnS Core/Shell Nanowires for Multifunctional Nanodevice Applications. *ACS Appl. Mater. Interfaces.* **2014**, *6*, 6170–6179.

(13) Mannhart, J.; Schlom, D. G. Oxide Interfaces—An Opportunity for Electronics. *Science* **2010**, *327*, 1607–1611.

(14) González, I.; Okamoto, S.; Yunoki, S.; Moreo, A.; Dagotto, E. Charge Transfer in Heterostructures of Strongly Correlated Materials. *J. Phys.: Condens. Matter* **2008**, *20*, 264002.

(15) Chakhalian, J.; Freeland, J. W.; Habermeier, H. U.; Cristiani, G.; Khaliulin, G.; Veenendaal, M. V.; Keimer, B. Orbital Reconstruction and Covalent Bonding at An Oxide Interface. *Science* **2007**, *318*, 1114–1117.

(16) Ding, M. N.; Sorescu, D. C.; Star, A. Photoinduced Charge Transfer and Acetone Sensitivity of Single-Walled Carbon Nanotube–Titanium Dioxide Hybrids. *J. Am. Ceram. Soc.* **2013**, *135*, 9015–9022.

(17) Tran, Q. T.; Hoa, H. T. M.; Yoo, D. H.; Cuong, T. V.; Hur, S. H.; Chung, J. S.; Kim, E. J. Reduced Graphene Oxide as An Over-

Coating Layer on Silver Nanostructures for Detecting NH$_3$ Gas at Room Temperature. *Sens. Actuators, B* **2014**, *194*, 45−50.

(18) Mao, S.; Lu, G. H.; Chen, J. H. Nanocarbon-Based Gas Sensors: Progress and Challenges. *J. Mater. Chem. A* **2014**, *2*, 5573−5579.

(19) Seo, J. W.; Jang, J. T.; Park, S. W.; Kim, C.; Park, B.; Cheon, J. Two-Dimensional SnS$_2$ Nanoplates with Extraordinary High Discharge Capacity for Lithium Ion Batteries. *Adv. Mater.* **2008**, *20*, 4269−4273.

(20) Ham, G.; Shin, S.; Park, J.; Choi, H.; Kim, J.; Lee, Y. A.; Seo, H.; Jeon, H. Tuning the Electronic Structure of Tin Sulfides Grown by Atomic Layer Deposition. *ACS Appl. Mater. Interfaces* **2013**, *5*, 8889−8896.

(21) Lu, G.; Ocola, L. E.; Chen, J. Room-Temperature Gas Sensing Based on Electron Transfer between Discrete Tin Oxide Nanocrystals and Multiwalled Carbon Nanotubes. *Adv. Mater.* **2009**, *21*, 2487−2491.

(22) Zhang, Y. C.; Du, Z. N.; Li, K. W.; Zhang, M.; Dionysiou, D. D. High-Performance Visible-Light-Driven SnS$_2$/SnO$_2$ Nanocomposite Photocatalyst Prepared via In situ Hydrothermal Oxidation of SnS2 Nanoparticles. *ACS Appl. Mater. Interfaces* **2011**, *3*, 1528−1537.

(23) Liu, Y.; Xie, C. S.; Li, H. Y.; Chen, H.; Zhou, T.; Zeng, D. W. Improvement of Gaseous Pollutant Photocatalysis With WO$_3$/TiO$_2$ Heterojunctional-Electrical Layered System. *J. Hazard. Mater.* **2011**, *196*, 52−58.

(24) Oskam, G. Metal Oxide Nanoparticles: Synthesis, Characterization and Application. *J. Sol-Gel Sci. Technol.* **2006**, *37*, 161−164.

(25) Greiner, M. T.; Chai, L.; Helander, M. G.; Tang, W. M.; Lu, Z. H. Metal/Metal-Oxide Interfaces: How Metal Contacts Affect the Work Function and Band Structure of MoO$_3$. *Adv. Funct. Mater.* **2013**, *23*, 215−226.

(26) Yang, D. J.; Kamienchick, I.; Youn, D. Y.; Rothschild, A.; Kim, I. O. Ultrasensitive and Highly Selective Gas Sensors Based on Electrospun SnO$_2$ Nanofibers Modified by Pd Loading. *Adv. Funct. Mater.* **2010**, *20*, 4258−4264.

(27) Huang, G.; Duan, L.; Dong, G.; Zhang, D.; Qiu, Y. High-Mobility Solution-Processed Tin Oxide Thin-Film Transistors with High-κ Alumina Dielectric Working in Enhancement Mode. *ACS Appl. Mater. Interfaces* **2014**, *6*, 20786−20794.

(28) Axnanda, S.; Zhu, Z.; Zhou, W.; Mao, B.; Chang, R.; Rani, S.; Crumlin, E.; Somorjai, G.; Liu, Z. In Situ Characterizations of Nanostructured SnO$_x$/Pt (111) Surfaces Using Ambient-Pressure XPS (APXPS) and High-Pressure Scanning Tunneling Microscopy (HPSTM). *J. Phys. Chem. C* **2014**, *118*, 1935−1943.

(29) Kuang, Q.; Zhou, X.; Zheng, L. S. Hexagonal ZnO/SnO$_2$ Core−Shell Micropyramids: Epitaxial Growth-Based Synthesis, Chemical Conversion, and Cathodoluminescence. *Inorg. Chem. Front.* **2014**, *1*, 186−192.

(30) Xu, K.; Zeng, D. W.; Wu, J. J.; Mao, Q. Q.; Tian, S. Q.; Zhang, S. P.; Xie, C. S. Correlation Between Microstructure and Gas Sensing Properties of Hierarchical Porous Tin Oxide Topologically Synthesized on Coplanar Sensors'Surface. *Sens. Actuators, B* **2014**, *205*, 416−425.

(31) Hsu, P. C.; Hsu, C. J.; Chang, C. H.; Tsai, S. P.; Chen, W. C.; Hsieh, H. H.; Wu, C. C. Sputtering Deposition of P-Type SnO Films with SnO$_2$ Target in Hydrogen-Containing Atmosphere. *ACS Appl. Mater. Interfaces* **2014**, *6*, 13724−13729.

(32) Zhang, Y. C.; Li, J.; Zhang, M.; Dionysiou, D. D. Size-Tunable Hydrothermal Synthesis of SnS$_2$ Nanocrystals with High Performance in Visible Light-Driven Photocatalytic Reduction of Aqueous Cr(VI). *Environ. Sci. Technol.* **2011**, *45*, 9324−9331.

(33) Zhang, Z.; Shao, C.; Li, X.; Sun, Y.; Zhang, M.; Mu, J.; Zhang, P.; Guo, Z.; Liu, Y. Hierarchical Assembly of Ultrathin Uexagonal SnS$_2$ Nanosheets onto Electrospun TiO$_2$ nanofibers: Enhanced Photocatalytic Activity Based on Photoinduced Interfacial Charge Transfer. *Nanoscale* **2013**, *5*, 606−618.

(34) Du, N.; Zhang, H.; Chen, B. D.; Ma, X. Y.; Liu, Z. H.; Wu, J. B.; Yang, D. R. Porous Indium Oxide Nanotubes: Layer-by-Layer Assembly on Carbon-Nanotube Templates and Application for

Room-Temperature NH$_3$ Gas Sensors. *Adv. Mater.* **2007**, *19*, 1641−1645.

(35) Korotcenkov, G. Metal Oxides for Solid-State Gas Sensors: What Determines Our Choice? *Mater. Sci. Eng. B* **2007**, *139*, 1−23.

(36) Gurlo, A.; Riedel, R. In Situ and Operando Spectroscopy for Assessing Mechanisms of Gas Sensing. *Angew. Chem., Int. Ed.* **2007**, *46*, 3826−3848.

(37) Law, M.; Kind, H.; Messer, B.; Kim, F.; Yang, P. Photochemical Sensing of NO$_2$ with SnO$_2$ Nanoribbon Nanosensors at Room Temperature. *Angew. Chem.* **2002**, *114*, 2511−2514.

(38) Zhang, Z.; Yates, J. T. Band Bending in Semiconductors: Chemical and Physical Consequences at Surfaces and Interfaces. *Chem. Rev.* **2012**, *112*, 5520−5551.

(39) Muraoka, Y.; Takubo, N.; Hiroi, Z. Photoinduced Conductivity in Tin Dioxide Thin Films. *J. Appl. Phys.* **2009**, *105*, 103702.

(40) Barsan, N.; Weimar, U. Conduction Model of Metal Oxide Gas Sensors. *J. Electroceram.* **2001**, *7*, 143−167.